Efficient Convex Optimization Approach to 3D Non-rigid MR-TRUS Registration

Yue Sun[1], Jing Yuan[1], Martin Rajchl[1], Wu Qiu[1], Cesare Romagnoli[2],
and Aaron Fenster[1,2]

[1] Imaging Research Labs, Robarts Research Institute, Western University, Canada
[2] Department of Medical Imaging, Western University, Canada

Abstract. In this study, we propose an efficient non-rigid MR-TRUS deformable registration method to improve the accuracy of targeting suspicious locations during a 3D ultrasound (US) guided prostate biopsy. The proposed deformable registration approach employs the multi-channel modality independent neighbourhood descriptor (MIND) as the local similarity feature across the two modalities of MR and TRUS, and a novel and efficient duality-based convex optimization based algorithmic scheme is introduced to extract the deformations which align the two MIND descriptors. The registration accuracy was evaluated using 10 patient images by measuring the TRE of manually identified corresponding intrinsic fiducials in the whole gland and peripheral zone, and performance metrics (DSC, MAD and MAXD) for the apex, mid-gland and base of the prostate were also calculated by comparing two manually segmented prostate surfaces in the registered 3D MR and TRUS images. Experimental results show that the proposed method yielded an overall mean TRE of 1.74 mm, which is favorably comparable to a clinical requirement for an error of less than 2.5 mm.

Keywords: Non-rigid Image Registration, Convex Optimization, MR-TRUS prostate registration, MIND Similarity Measurement.

1 Introduction

Prostate cancer is the most common non-skin cancer in men of developed countries, with a large and increasing incidence in most countries, and the third leading cause of death due to cancer. It is estimated to affect 26,500 men in Canada in 2012 [1], 238,590 in United States in 2013 [2] and is the most common cancer in men in UK (40,975 new cases in 2010) [3]. To this end, transrectal ultrasound (TRUS) guided prostate biopsy is the standard approach for definitive diagnosis and guiding biopsy needles to suspicious regions in the prostate, due to its real-time and radiation-free imaging capability, low cost and operation simplicity [4]. However, its lack of image contrast to clearly visualize early-stage prostate cancer results in false-negative rates for systematic sextant biopsies ranging up to 30% [5] and thereby increasing the number of repeat biopsies.

Recent developments in Magnetic Resonance Imaging (MRI) have demonstrated a high sensitivity and specificity for the detection of early stage prostate

K. Mori et al. (Eds.): MICCAI 2013, Part I, LNCS 8149, pp. 195–202, 2013.

cancer [6]. Reports have shown that MRI can achieve a high accuracy of diagnosing prostate cancer at approximately 72-76% [7]. Although MR prostate imaging is advancing, it cannot yet replace TRUS guided needle biopsy, especially when real-time guidance is required, due to the high cost and time consuming procedure associated with performing MR imaging and targeting. In this regard, MR-TRUS registration technique provides an effective way to use TRUS to target biopsy needles toward regions of the prostate containing MR identified suspicious lesions [8]. However, efficient and accurate 3D non-rigid MR-TRUS registration is a challenging task due to the totally different image appearances of these two image modalities, in spite of its great clinical interests in practice. Few works to date have contributed to this task. Hu *et al.* [9] used a patient-specific finite element-based statistical motion model trained by biomechanical simulations and registered the model to 3D TRUS images, which was done by maximizing the likelihood of a particular model shape given a voxel intensity-based feature that provided an estimate of surface normal vectors at the boundary of the gland. Mitra *et al.* [10] proposed a 2D thin-plate spline-based non-linear regularization approach to align the sampled points of the segmented prostate contours, which essentially match the Bhattacharyya distance of the applied statistical shape contexts; however, the proposed framework only worked in 2D, which limits its application in practice.

Contributions: In this work, we propose a novel duality-based approach to computing the challenging 3D MIND-based non-rigid MR-TRUS deformable registration. A coarse-to-fine scheme is applied to capture the large deformations, and at each resolution level, an efficient multiplier-based algorithm is employed to compute an updated incremental deformation field. We performed the proposed method to register 10 patient images. Our results demonstrate that the proposed method yields clinically sufficient accuracy with less user interactions, while the segmentation of prostate boundaries is not required. A mean TRE of 1.74 mm is obtained, which is favorably comparable to a clinical requirement for an error of less than 2.5 mm.

2 Method

The modality independent neighbourhood descriptor (MIND) introduced by Heinrich *et al.* [11] presents an image descriptor independent of the modality, contrast and noise of various image modalities, while sensitive to the inherent image features such as image corners or edges etc. It is actually based on the local image self-similarity feature, which was originally introduced by Buades *et al.* [12] for image denoising. In [11], Heinrich *et al.* demonstrated for image registration, especially with different image modalities, the point-wise MIND descriptor performs superior to the other proposed image information descriptors, such as the normalized mutual information (NMI) [13] or patch-based entropy descriptor [14] etc. In this work, we utilize MIND as the cross-modality measure to the introduced 3D non-rigid MR-TRUS deformable registration. Let $I^M(x)$ and $I^R(x)$ be the input 3D MR image and TRUS image respectively.

$\mathcal{M}(x) := (m_1(x), \ldots, m_k(x))^{\mathrm{T}}$ and $\mathcal{R}(x) := (r_1(x), \ldots, r_k(x))^{\mathrm{T}}$ be the computed k-channel MIND descriptor at x associated with the MR image $I^M(x)$ and the TRUS image $I^R(x)$, where k is the dimension of the applied MIND descriptor. We aim to minimize a difference measure between $\mathcal{M}(x)$ and the deformed $\mathcal{R}(x+u)$ over the deformation field $u(x) = (u_1(x), u_2(x), u_3(x))^{\mathrm{T}}$, which can be essentially formulated as

$$\min_u \; P(\mathcal{M}(x), \mathcal{R}(x+u)) \; := \; \sum_{i=1}^{k} \int p_i(m_i(x) - r_i(x+u))\, dx\,, \tag{1}$$

where the penalty function $p_i(v)$, $i = 1 \ldots k$, is often positive and convex. For example, when $p_i(v) = |v|^2/2$, $i = 1 \ldots k$, the above formulation defines the sum of squared difference measure (SSD). Clearly, the minimization of (1) is ill-posed, for which a smoothness regularization of the deformation field $u(x)$ is often added to (1) to restrict the solution space of $u(x)$. In this paper, we consider the convex regularization term $G(u) := \sum_{i=1}^{3} \int |\nabla u_i|^2 \, dx$, which results in the following minimization problem

$$\min_u \; P(\mathcal{M}(x), \mathcal{R}(x+u)) \; + \; \alpha\, G(u) \tag{2}$$

where $\alpha > 0$ is constant.

2.1 Linearization and Primal-Dual Optimization Approach

Note the function $\mathcal{R}(x+u)$ is often highly non-smooth, hence the energy function of (2). To efficiently address the challenging minimization problem of (2), we first linearize and approximate $\mathcal{R}(x+u) := (r_1(x+u), \ldots, r_k(x+u))$ by

$$r_i(x+u) \; \simeq \; (r_i + \nabla r_i \cdot u)(x)\,, \quad i \; = \; 1 \ldots k\,. \tag{3}$$

Therefore, we have the linearized approximation of (2) which amounts to

$$\min_u \; \sum_{i=1}^{k} \int p_i\Big(\big((m_i - r_i) - \nabla r_i \cdot u\big)(x)\Big)\, dx \; + \; \alpha\, G(u)\,. \tag{4}$$

Let $p_i^*(w)$, $i = 1 \ldots k$, be the conjugate of the convex function $p_i(v)$ such that

$$p_i(v_i(x)) \; = \; \max_{w_i(x)} \; v_i(x) \cdot w_i(x) \; - \; p_i^*(w_i(x))\,. \tag{5}$$

However, we also have

$$\alpha\, G(u) \; = \; \max_q \sum_{j=1}^{3} \langle \operatorname{div} q_j, u_j \rangle \; - \; \frac{1}{2\alpha} \sum_{j=1}^{3} \int q_j^2(x)\, dx\,. \tag{6}$$

In view of (3)-(6), through simple computation, we have the following *dual formulation* to the convex minimization problem (4):

$$\max_{w,q} \; E(w,q) \; := \; \sum_{i=1}^{k} \langle w_i, m_i - r_i \rangle \; - \; \sum_{i=1}^{k} \int p_i^*(w_i(x))\, dx \; - \; \frac{1}{2\alpha} \sum_{j=1}^{3} \int q_j^2(x)\, dx \tag{7}$$

subject to

$$F_j(x) := \sum_{i=1}^{k} w_i(x) \cdot \partial_j r_i(x) - \operatorname{div} q_j(x) = 0 ; \quad j \in \{1, 2, 3\} , \ \forall x \in \Omega . \quad (8)$$

By modern convex optimization theories, it is easy to prove that

Proposition 1. *The* convex minimization problem (4) *and the* dual optimization formulation (7) *are equivalent to each other, i.e.* (4) $\Longleftrightarrow$ (7)*.*

In fact, each component of the deformation field $(u_1(x), u_2(x), u_3(x))^{\mathrm{T}}$ just works as the multiplier function to the respective linear equalities (8) under the perspective of primal and dual. Therefore, we can derive an efficient duality-based Lagrangian augmented algorithm, see [15,16] for details of the modern dual optimization theory and applications in image processing.

2.2 Coarse-to-Fine Incremental Scheme

To capture the large deformations, a coarse-to-fine scheme is applied. First, we construct a coarse-to-fine pyramid of each MIND descriptor function: let $\mathcal{M}^1(x) \ldots \mathcal{M}^L(x)$ be the L-level coarse-to-fine pyramid representation of $\mathcal{M}(x)$ from the coarsest resolution $\mathcal{M}_1(x)$ to the finest resolution $\mathcal{M}^L(x) = \mathcal{M}(x)$; and $\mathcal{R}^1(x) \ldots \mathcal{R}^L(x)$ the L-level coarse-to-fine pyramid representation of $\mathcal{R}(x)$.

At each ℓ level, $\ell = 1 \ldots L$, we compute the deformation field $u^\ell(x)$ based on the two MIND functions $\mathcal{M}^\ell(x)$ and $\mathcal{R}^\ell(x + u^{\ell-1})$ at the same resolution level, where $\mathcal{R}^\ell(x + u^{\ell-1})$ is warped by the deformation field $u^{\ell-1}(x)$ computed at the previous level $\ell - 1$. For the coarsest level, i.e. $\ell = 1$, the so-called previous-level deformation is set to be 0.

3 Experiments and Evaluation

Manual Initialization. The MR image is first resampled to have the same dimensions and voxel size as the TRUS image. We initialize the registration using 3 manually placed approximately corresponding landmarks and the centroid of the three points as a default point on the 3D TRUS and MR images to generate a rigid transform as initial alignment. These manually selected landmarks are closely associated with geometric features that can be observed on both modalities. Fig. 1 shows an example of the landmarks on the prostate boundary on the axial MR and 3D TRUS slices, which correspond to the image with the largest view of the prostate.

Materials. In this study, T2-weighted MR images using a body coil and corresponding 3D TRUS images from 10 patients were acquired. The MR images were obtained at 3 Tesla using a GE Excite HD MRI system (Milwaukee, WI, USA) at an image size of 512 × 512 × 36 voxels with a voxel size of 0.27 × 0.27 × 2.2 mm^3. The 3D TRUS images were acquired using a 3D TRUS mechanical scanning system developed in our laboratory, using a Philips HDI-5000 US machine with a Philips C9-5 transducer. The 3D TRUS image size is 448 × 448 × 350 voxels with a voxel size of 0.19 × 0.19 × 0.19 mm^3.

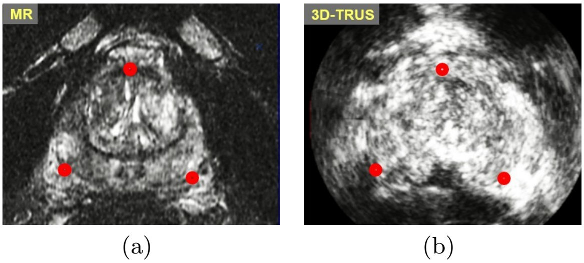

(a) (b)

Fig. 1. Red dots indicate corresponding anatomical landmarks on the MR (a) and TRUS images (b)

Evaluation. We measured the target registration error (TRE) as the overall misalignment of manually marked corresponding intrinsic fiducials in MR and 3D TRUS images. We selected 41 fiducial pairs, of which 17 were within the peripheral zone (PZ), in which up to 80% of the tumors can be located. The PZ is subject to the deformation caused by the US transducer during the biopsy, which must be corrected to allow accurate biopsy targeting. We also measured the fiducial localization error (FLE) [17] to allow determination whether fiducial identification dominates the TRE. We also compared the registered MR and corresponding 3D TRUS images by calculating the Dice similarity coefficient (DSC) [18], the mean absolute surface distance (MAD), and the maximum absolute surface distance (MAXD) [19]. All validation metrics were separately calculated for three prostate sub-regions: the apex, mid-gland and base, selected along the apex-base axis of the manual segmented TRUS prostates (0.3, 0.4, 0.3 of the length of the base-apex axis respectively) [20].

Accuracy. The frequency distributions of the TREs for the PZ, central gland (CG) and whole gland (WG) are plotted in Figure 3 and the mean TRE results are summarized in Table 1. The results of FLE are 0.21 mm for 3D TRUS and 0.18 mm for MR. Table 2 shows the mean DSC, MAD and MAXD for WG, apex, mid-gland, and base, respectively.

Computation Time. The proposed non-rigid MR-TRUS registration algorithm was implemented using parallel computing architecture (CUDA, NVIDIA Corp., Santa Clara, CA), and the user interface was developed in Matlab (Natick, MA). The experiments were conducted on a Windows desktop with an Intel i7-3770 CPU (3.4 GHz) and a GPU of NVIDIA Geforce 680GTX. The mean registration time of our method per patient was $90 \pm 5s$ in addition to $30 \pm 5s$ for initialization.

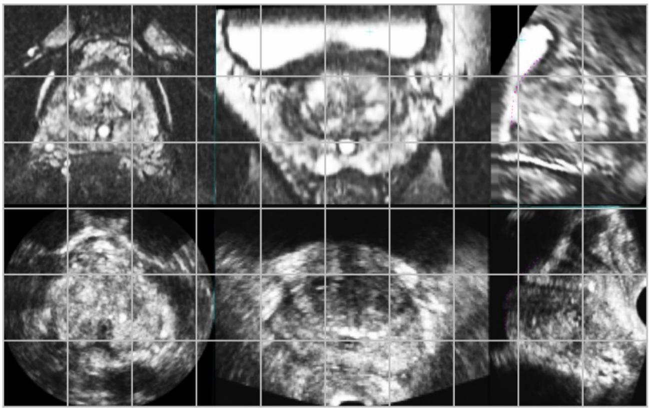

Fig. 2. Examples of axial (left column), coronal (middle column) and sagittal (right column) views through registered MR (top row) and 3D TRUS (bottom row) images

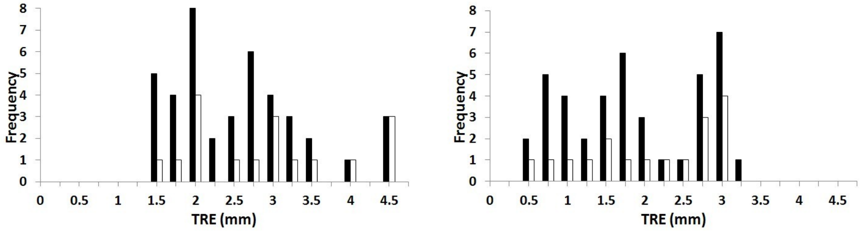

(a) (b)

Fig. 3. WG (black) and PZ (white) frequency distributions of: (a) initial alignment TRE between all 41 fiducial pairs, and (b) non-rigid registration TRE

Table 1. Peripheral zone (PZ), central gland (CG) and whole gland (WG) mean TRE results for non rigid MR-TRUS registration

	PZ	CG	WG
TRE (mm)	1.97 ± 0.86	1.58 ± 0.82	1.74 ± 0.84

Table 2. Results of DSC, MAD and MAXD for 10 patient images

	Apex	Mid	Base	WG
DSC (%)	83.0 ± 5.6	92.9 ± 2.6	80.1 ± 4.7	85.6 ± 2.5
MAD (mm)	2.09 ± 0.69	1.36 ± 0.44	2.38 ± 0.63	1.79 ± 0.36
MAXD (mm)	9.22 ± 2.84	4.81 ± 0.76	10.12 ± 2.99	7.86 ± 2.99

4 Discussion and Conclusion

In this work, we propose a convex optimization approach to non-rigid image-based MR-TRUS registration, which yielded PZ, CG and WG TRE values of 1.97 mm, 1.58 mm and 1.74 mm respectively (less than the clinically acceptable maximum TRE of 2.5 mm [21]). The higher value in PZ is due to the deformation caused by the US probe. Figure 3(b) shows that 80% of the TRE values for WG and 76% for PZ are below the desired values. The FLE was 0.21 mm for 3D TRUS images, and 0.18 mm for MR. Thus, the FLEs did not dominate the overall TRE. Table 2 shows that the proposed method generated a favorable DSC value of $92.9 \pm 2.6\%$ for the mid-gland, $83.0 \pm 5.6\%$ for the apex, and $80.1 \pm 4.7\%$ for the base. The lower DSC values for the apex and base compared to the mid-gland were caused by the low degree of structure recognition in these regions for MR and especially TRUS images. In addition, our method delivers similar consistent results of MAD and MAXD to the DSC. The mean TRE of 1.74 ± 0.84 mm is higher than the value of 1.60 ± 1.17 mm in Mitra *et al.* [10]. However, their method needed a segmented prostate surface for both MR and TRUS images, and also required the established MR-TRUS slice correspondence, which is difficult to achieve in practice. A median Root Mean Square (RMS) TRE of 2.4 mm was achieved in Hu *et al.* [9]; however, their biomechanical modeling required the additional segmentations of the MR prostate gland and lesion for the assistance (about 45 mins per patient).

In conclusion, to reduce the false negative rate for prostate biopsy, we developed an alternate approach using 3D TRUS images registered with MR images with targets identified to guide the biopsy. An efficient dual optimization approach is proposed to extracting the non-rigid MR-TRUS deformation field by registering the given two MIND descriptors, which does not require the segmentation of the prostate boundaries. Experimental results demonstrate that the proposed method yields clinically sufficient accuracy with less user interactions. In computation, once the deformation field is discretized, a dynamic prima-dual scheme [22] can also be adapted to extract the discrete-valued voxelwise correspondences.

Acknowledgements. The authors are grateful for the funding support from the Canadian Institutes of Health Research (CIHR), the Ontario Institute of Cancer Research (OICR), and the Canada Research Chairs (CRC) Program.

References

1. Canadian Cancer Society (2012), `http://www.cancer.ca`
2. National Cancer Institute (2012), `http://www.cancer.gov`
3. Cancer Research UK (2013), `http://www.cancerresearchuk.org`
4. Rifkin, M.: Ultrasound of the prostate: imaging in the diagnosis and therapy of prostatic disease. Lippincott-Raven Publishers (1997)
5. Norberg, M., Egevad, L., Holmberg, L., Sparén, P., Norlén, B., Busch, C.: The sextant protocol for ultrasound-guided core biopsies of the prostate underestimates the presence of cancer. Urology 50(4), 562–566 (1997)

6. Zakian, K.L., Sircar, K., Hricak, H., Chen, H.N., Shukla-Dave, A., Eberhardt, S., Muruganandham, M., Ebora, L., Kattan, M.W., Reuter, V.E., Scardino, P.T., Koutcher, J.A.: Correlation of proton MR spectroscopic imaging with gleason score based on step-section pathologic analysis after radical prostatectomy. Radiology 234(3), 804–814 (2005)
7. Vilanova, J., Barceló-Vidal, C., Comet, J., Boada, M., Barceló, J., Ferrer, J., Albanell, J.: Usefulness of prebiopsy multifunctional and morphologic MRI combined with free-to-total prostate-specific antigen ratio in the detection of prostate cancer. American Journal of Roen 196, W715–W722 (2011)
8. Sonn, G.A., Natarajan, S., Margolis, D.J., MacAiran, M., Lieu, P., Huang, J., Dorey, F.J., Marks, L.S.: Targeted biopsy in the detection of prostate cancer using an office based magnetic resonance ultrasound fusion device. The Journal of Urology 189(1), 86–92 (2013)
9. Hu, Y., Ahmed, H.U., Taylor, Z., Allen, C., Emberton, M., Hawkes, D., Barratt, D.: MR to ultrasound registration for image-guided prostate interventions. Medical Image Analysis 16(3), 687–703 (2012)
10. Mitra, J., Kato, Z., Marti, R., Oliver, A., Llad, X., Sidib, D., Ghose, S., Vilanova, J.C., Comet, J., Meriaudeau, F.: A spline-based non-linear diffeomorphism for multimodal prostate registration. Medical Image Analysis 16(6), 1259–1279 (2012)
11. Heinrich, M.P., Jenkinson, M., Bhushan, M., Matin, T., Gleeson, F.V., Brady, S.M., Schnabel, J.A.: Mind: Modality independent neighbourhood descriptor for multi-modal deformable registration. MedIA 16(7), 1423–1435 (2012)
12. Buades, A., Coll, B., Morel, J.M.: A non-local algorithm for image denoising. In: CVPR, pp. 60–65 (2005)
13. Hermosillo, G., Chefd'Hotel, C., Faugeras, O.D.: Variational methods for multimodal image matching. International Journal of Computer Vision 50(3), 329–343 (2002)
14. Wachinger, C., Navab, N.: Entropy and laplacian images: Structural representations for multi-modal registration. Medical Image Analysis 16(1), 1–17 (2012)
15. Yuan, J., Bae, E., Tai, X.: A study on continuous max-flow and min-cut approaches. In: CVPR (2010)
16. Yuan, J., Bae, E., Tai, X.-C., Boykov, Y.: A continuous max-flow approach to potts model. In: Daniilidis, K., Maragos, P., Paragios, N. (eds.) ECCV 2010, Part VI. LNCS, vol. 6316, pp. 379–392. Springer, Heidelberg (2010)
17. Fitzpatrick, J., West, J., Maurer Jr., C.R.: Predicting error in rigid-body point-based registration. IEEE TMI 17(5), 694–702 (1998)
18. Zou, K., Warfield, S., Bharatha, A., Tempany, C., Kaus, M., Haker, S., Wells, W., Jolesz, F., Kikinis, R.: Statistical validation of image segmentation quality based on a spatial overlap index. Academic Radiology 11(2), 178–189 (2004)
19. Qiu, W., Yuan, J., Ukwatta, E., Tessier, D., Fenster, A.: Rotational-slice-based prostate segmentation using level set with shape constraint for 3D end-firing TRUS guided biopsy. In: Ayache, N., Delingette, H., Golland, P., Mori, K. (eds.) MICCAI 2012, Part I. LNCS, vol. 7510, pp. 537–544. Springer, Heidelberg (2012)
20. Mahdavi, S.S., Chng, N., Spadinger, I., Morris, W.J., Salcudean, S.E.: Semi-automatic segmentation for prostate interventions. Medical Image Analysis 15(2), 226–237 (2011)
21. Karnik, V., Fenster, A., Bax, J., Cool, D., Gardi, L., Gyacskov, I., Romagnoli, C., Ward, A.: Assessment of image registration accuracy in three-dimensional transrectal ultrasound guided prostate biopsy. Medical physics 37, 802 (2010)
22. Komodakis, N., Tziritas, G., Paragios, N.: Fast, approximately optimal solutions for single and dynamic MRFs. In: CVPR (2007)